

An ensemble Synthetic Eddy Method for accurate treatment of inhomogeneous turbulence

Kyle A. Schau ^{*}, Chelsea Johnson, Julia Muller, Joseph C. Oefelein

Daniel Guggenheim School of Aerospace Engineering, Georgia Institute of Technology, Atlanta, GA, United States of America



ARTICLE INFO

Keywords:

Synthetic eddy method
Inflow turbulence generation
Turbulence modeling
Large eddy simulation
Computational fluid dynamics

ABSTRACT

An ensemble approach to generating turbulent inflow boundary conditions using the Synthetic Eddy Method is proposed that improves signal accuracy in recovering target statistics for inhomogeneous turbulence while reducing the cost of generating an inflow signal. This is accomplished by eliminating typical restrictions related to the Synthetic Eddy Method such as homogeneous turbulence, limited shape functions, random eddy placement, and uniform synthetic eddy convection velocity. The approach gives flexibility and freedom to prescribe arbitrary synthetic eddy length scales, shape functions, eddy placement, and convective velocities while accurately reproducing input Reynolds stresses and maintaining the simplicity of the original method. Three examples of leveraging this flexibility to provide accurate turbulent length scale inhomogeneity and reduce the required number of generated synthetic eddies are provided. Turbulent inflow signals for a channel flow configuration are generated using six variations and the resulting signal accuracy and costs are compared. These inflow signals are applied to a set of Large Eddy Simulations of turbulent channel flow and show favorable results over the original method in terms of the skin friction coefficient convergence, Q-criterion plots, and computed Reynolds stresses. The ensemble approach is shown to be more accurate in reproducing desired turbulent characteristics compared to the original Synthetic Eddy Method, in a simpler manner compared to recent variants of the method.

1. Introduction

With the increase in computational power and availability, computational fluid dynamics (CFD) calculations such as LES and Direct Numerical Simulation (DNS) have become widely used tools in research and industry to study turbulent flows. In contrast to Reynolds-Averaged Navier–Stokes (RANS) calculations, in which the time-averaged Navier–Stokes equations are solved, LES and DNS calculations are time accurate, and can capture the unsteady broadband dynamics of interest in turbulent flows. The simulation of turbulent flow can be achieved through specification of a uniform or laminar inlet boundary condition that is allowed to transition naturally, or is forced (tripped) into turbulent flow. The natural transition approach requires additional geometry and computer resources for the flow to transition into turbulent flow, the cost of which can be significant [1]. Accordingly, it is often useful or necessary to prescribe time dependent boundary conditions to LES and DNS calculations. In particular, simulation of turbulent flows can benefit from the application of a time-accurate spatially-correlated velocity field boundary condition at the inlet of numerical domains. An accurate fluctuating signal (in this paper the term *signal* refers to the fluctuating velocity field prescribed to an inlet) starts the imposed

boundary condition closer to the desired turbulent inflow conditions. The specification of more precise turbulent inlet signals can result in smaller computational domains and shorter error-dispersion regions downstream of the inlet. As long as key information is known about the turbulence characteristics, one can generate an accurate signal to approximate the behavior of a turbulent flow field. The benefits of using an accurate signal are especially important when attempting to match flow domain conditions of reference experiments, applications, or simulations at specific locations.

Implementing both a precise and computationally efficient turbulent inflow signal has been an active area of research for decades. According to Tabor and Bada-Ahmadi [2], methods fit into two categories: (1) the use of precursor simulation data via rescaling or direct application, or (2) the generation of a unique signal based on some algorithm. The most prevalent method of the former is the Recycling–Rescaling method popularized by Lund [3]. For this method, an instantaneous flow field from a precursor simulation, or downstream of the inlet plane in the main simulation, is “recycled” for use at an inlet plane. These methods result in very accurate and realistic signals that can easily be adapted to satisfy mass conservation equations or

^{*} Corresponding author.

E-mail address: kschau@gatech.edu (K.A. Schau).

Nomenclature	
a_{ij}	Cholesky decomposition of the Reynolds stress tensor, R_{ij}
C_{eddy}	Scale factor of eddy population
δ	Channel half height
e_{ij}	Error between target Reynolds stress component and generated signal one-point statistics
ϵ_k	Intensity sign of k th eddy
$f(x')$	Synthetic eddy shape function
N	Number of synthetic eddies in eddy volume
R_{ij}	One-point statistics, Reynolds stress tensor
σ_{ij}	Eddy length scale of the i th velocity component in the j th coordinate direction
t_E	Ensemble signal time
V_B	Volume of eddy volume
V_{eddy}	Volume of synthetic eddy
u_i	Velocity fluctuation signal of i th velocity component
u_i^*	Un-normalized signal of i th velocity component
u, v, w	Velocity fluctuation in the streamwise, wall-normal, and spanwise directions, respectively
\bar{U}_i	Mean velocity of the i th velocity component
U_c	Channel center line velocity, synthetic eddy convection velocity
x_i	Spatial dimensions
x, y, z	Spatial dimensions in the streamwise, wall-normal, and spanwise directions, respectively
$\langle \cdot \rangle$	Time average operation

divergence free assumptions. However, the requirement of precursor simulations adds additional expense, and the re-use of downstream data at the inlet introduces spurious periodicity [1]. Additionally, the recycling–rescaling approach limits the extension to new or more complex boundary conditions.

In contrast to precursor methods, the algorithmic creation of turbulent inflow signals is limited in terms of physical realism. The generated signal does not satisfy the Navier–Stokes equations and is simplified from real turbulence. However, this approach can be computationally inexpensive and is flexible when extended to different boundary conditions. The primary strategy is to generate a signal that reproduces key time- and length-scales of turbulence and related statistical quantities such as the Reynolds stresses. Thus, an algorithmic method will require target length-scales (or frequency content) and target statistics. As this information is not always available for an arbitrary geometry or flow condition, one can make simplifying assumptions about the targeted turbulence. The trade-off being, the generated inflow signal is only as accurate as the input data. Tabor and Bada-Ahmadi [2] categorize algorithmic signal generation into four groups: (1) Fourier methods, (2) proper orthogonal decomposition (POD) methods, (3) digital filter methods, and (4) convection of spatially coherent fluctuation functions. Fourier methods target turbulent spectra by creating signals from harmonic functions with random coefficients. Since each harmonic function has a known frequency content, the signals can be tailored to a desired turbulent spectra. Originally developed for isotropic turbulence by Kraichan [4], it has been extended to anisotropic turbulence by Smirnov et al. [5], generalized to arbitrary grids and inlets by Batton et al. [6], and improved in accuracy by Patterson et al. [7].

POD methods can be viewed as a hybrid approach between precursor simulation and algorithmic signal generation. Precursor simulation or experimental data is decomposed into a set of basis functions that represent the original data set. Druault et al. [8] used this method for creation of DNS/LES inflow signals using hot-wire measurements from experiments. The digital filtering method was first developed by Klein et al. [9]. Beginning with a random signal, the digital filtering approach applies successive filters to the random data to drive the signals toward desired spatio-temporal coherence and Reynolds stresses. Di Mare et al. [10] extended the original digital filtering approach to include longitudinal Reynolds stress targeting with a single length scale, and a complete Reynolds stress tensor with inhomogeneous length scale specification.

The final category of algorithmic signal generation is the convection of spatially coherent fluctuating functions. Originating from the Vortex Method [11], the most popular version being the SEM of Jarrin [12], these methods convect spatially coherent fluctuation functions (referred to as eddies) across an inlet boundary plane. The fluctuating velocity signal resulting from the superposition of these eddies is then scaled such that the signal approaches desired Reynolds stresses in a statistical limit. Both the Fourier and digital filtering methods and the SEM targets the two-point statistics of an autocorrelation function. Since the turbulent spectrum and autocorrelation functions are related by a Fourier transform [13], the methods can achieve similar results in terms of spatial and temporal correlation and frequency content. More details of the evolution and improvements of the SEM will be discussed in Section 2. More comprehensive reviews of the above methods, and others, can be found in [1,2,14].

The conceptual simplicity of the oSEM provides potential advantages over the other methods mentioned above. Any algorithm-based method must not only produce desirable signals, but also integrate efficiently and seamlessly into a simulation code, which is often developed within a parallel computational framework. However, the formulation of the oSEM has strict requirements to ensure it reproduces the input second-order, one-point statistics. These requirements can inhibit extending the method across a broader range of flow configurations. This paper focuses on increasing the flexibility of the SEM to improve the accuracy and cost of generating turbulent inflow signals while maintaining the simplicity and ease of implementation of the oSEM. Section 2 provides a brief overview of the oSEM and describes previous improvements to the method. Section 3 proposes an ensemble approach to the SEM that provides increased flexibility to the method. Section 4 introduces means of leveraging the flexibility of the proposed method and compares the accuracy and cost of the method with others. Finally, Section 5 provides simulation results from the proposed method for a turbulent channel flow.

2. Original Synthetic Eddy Method

The oSEM computes turbulent fluctuation components, u'_i , to be superimposed onto a mean velocity profile, $u_i = \bar{U} + u'_i$. The fluctuation components are modeled as Lagrangian particles, referred to as “eddies”, convecting past the inlet boundary of an LES or DNS flow domain at a uniform convective velocity, U_c . Each eddy has a location, $\mathbf{x}_k = (x_k, y_k, z_k)$ in which the x coordinate changes with simulation time via a frozen-turbulence analogy, $\Delta x = U_c \Delta t$, where Δt is the time step of the simulation. Eddies exist within an “eddy volume” that surrounds the inlet plane. As eddies provide the fluctuating components of the signal, a sufficient number of eddies must exist within the eddy volume to provide coverage for the entire inlet boundary. As an eddy convects out of the eddy volume and no longer contributes to the inlet signal, a new eddy is generated with random position at the upstream-most face of the eddy volume. A pictorial representation of the oSEM is in Fig. 1.

Each k th eddy is randomly assigned a fluctuation sign for each j th velocity component, $(\epsilon_j)_k \in \{-1, 1\}$, signifying whether the k th eddy contributes positively or negatively to the j th computed fluctuation

signal. Further, eddies have an *extent of spatial influence*, σ , analogous to a length scale of a physical eddy. An eddy's length scale determines how far from the eddy location, x_k , the eddy will contribute to a signal. This length scale also serves to define the two-point correlation functions (and related energy spectra), in both space and time, targeted by the generated signals. At any instant in time the sum of all contributing eddies to a point on the inlet plane, (x, y, z) , is:

$$u_i^*(x, y, z) = \sum_{k=1}^N (\epsilon_i)_k \left[f\left(\frac{x - x_k}{\sigma}\right) f\left(\frac{y - y_k}{\sigma}\right) f\left(\frac{z - z_k}{\sigma}\right) \right], \quad (1)$$

where N is the total number of eddies in the eddy volume and $f(x')$ is a shape function. The purpose of the shape function is to provide a functional relationship between the magnitude of an eddy's contribution to a signal, the length scale σ , and the distance between the inlet point and eddy center. The oSEM requires the shape function have compact support over the length scale, σ , and satisfy the normalization

$$\int [f(x')]^2 dx' = 1. \quad (2)$$

A common choice for $f(x')$ is the tent function

$$f(x') = \begin{cases} \sqrt{\frac{3}{2}}(1 - |x'|) & |x'| < 1 \\ 0 & |x'| > 1 \end{cases}. \quad (3)$$

The signal in Eq. (1) represents the un-normalized signal comprised of the superposition of all contributing eddies at a given location on the inlet plane. This un-normalized signal is an important quantity for understanding both the capabilities and limitations of the oSEM. The un-normalized signal, u_i^* , is already correlated in both space and time. To match the specified one-point statistics, u_i^* must be normalized and multiplied by the Cholesky decomposition of the Reynolds stress tensor as follows

$$u_i = a_{ij} \sqrt{\frac{V_B}{N\sigma^3}} u_j^*, \quad (4)$$

where V_B is the volume of the eddy volume, the term σ^3 is the volume of a homogeneous eddy, and a_{ij} represents components of the Cholesky decomposition of the Reynolds stress tensor, R_{ij} ,

$$a_{ij} = \begin{pmatrix} \sqrt{R_{11}} & 0 & 0 \\ R_{21}/a_{11} & \sqrt{R_{22} - a_{21}^2} & 0 \\ R_{31}/a_{11} & (R_{32} - a_{21}a_{31})/a_{22} & \sqrt{R_{33} - a_{31}^2 - a_{32}^2} \end{pmatrix}. \quad (5)$$

The Reynolds stress tensor can vary with position (e.g., distance from the wall) to provide realistic inhomogeneity in one-point statistics (e.g., in wall bounded flows). The properties of the Cholesky decomposition ensure the final signal approaches the input one-point statistic tensor, R_{ij} , in a statistical limit, provided the following criteria are met:

Requirements for Cholesky Decomposition

- The un-normalized signal, u_i^* , of Eq. (1) approaches zero mean.
- The components of the un-normalized signal, u_i^* , approach zero covariance, or cross-correlation.
- The normalized signal $\sqrt{\frac{V_B}{N\sigma^3}} u_j^*$ approaches unit variance.

Since the inflow signal is created as the simulation progresses in time, there is a convergence rate associated with the generated signal toward its desired one-point statistics. In practice, the above criteria place limitations on the construction of the oSEM algorithm [12], namely:

Algorithmic Restrictions on the oSEM

1. To achieve zero mean for u_i^* , the fluctuation signs, ϵ_k , must be independent from one another such that $\langle \epsilon_k \rangle = 0$.

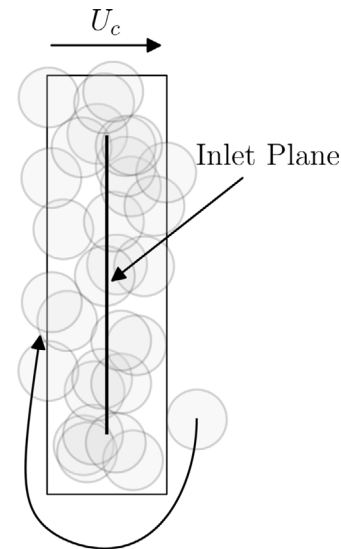


Fig. 1. Pictorial representation of the eddy volume and the Synthetic Eddy Method.

2. To achieve zero covariance between components u_i^* and u_j^* , the fluctuation signs must be independently assigned such that $\langle \epsilon_i \epsilon_j \rangle = 0$.
3. To achieve unit variance, the "eddy density" must be consistent everywhere inside the eddy volume and well approximated by the ratio $\frac{V_B}{N\sigma^3}$.

The normalization factor associated with item (3) in *Algorithmic Restrictions* the oSEM represents the numerical integration of Eq. (2) and ensures

$$\left\langle \left[\sqrt{\frac{V_B}{N\sigma^3}} u_i^* \right]^2 \right\rangle = 1. \quad (6)$$

In order to achieve unit variance of u_i^* the following requirements are necessary:

oSEM Requirements for Unit Variance of u_i^*

- The eddy locations must be independent and random in space such that the number of eddies contributing to each inlet point is the same (on average) across the inlet boundary for the entire signal.
- The eddy length scales must be homogeneous to avoid varying eddy density.
- The eddies must contribute to a signal via a shape function adhering to the normalization of Eq. (2).
- The eddies must all convect at the same velocity to avoid an accumulation of eddies in regions of slower convective velocities, corrupting a uniform eddy density.

If all of the criteria listed in *Algorithmic Restrictions on the oSEM* are met, the oSEM will converge to the prescribed one-point statistics in a statistical limit (at a rate essentially controlled by the convergence of random numbers to zero mean). Note the Cholesky decomposition can have a detrimental effect on the spatial coherence of the signal obtained from Eq. (4). However the impact of this is generally minimal. See [Appendix A](#) for more details on this aspect.

2.1. Limitations of the oSEM

The requirement of homogeneous length scales in the oSEM is especially problematic for inhomogeneous turbulent flows. In wall bounded flows, for example, variations in turbulent length scales and structures

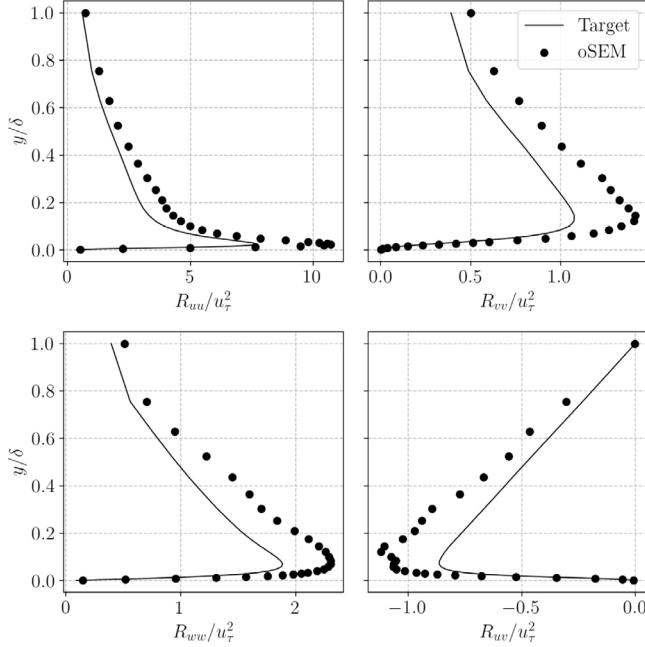


Fig. 2. Generated one-point statistics of the original SEM using an inhomogeneous length scale prescription against target values.

significantly contribute to the dynamics of the flow. Applying inhomogeneous length scales to the oSEM to account for inhomogeneities, however, raises key questions. *How far should the eddy volume extend beyond the inlet domain when the eddy length scales vary with distance from the wall? What should the total number of eddies, N , in the eddy volume be in Eq. (4) for a random placement of inhomogeneous eddies that guarantees varying eddy density? How does one calculate σ^3 in Eq. (4) for inhomogeneous eddies?* These questions do not have general answers that are extendable to arbitrary length scale specifications. The application of inhomogeneous length scales corrupts the normalization of Eq. (4) and therefore the accuracy of the resulting one-point statistics are corrupted (i.e., statistics associated with the output signal will not match the input statistics used to generate the signal). An example of this discrepancy is illustrated in Fig. 2, which shows span averaged one-point statistics of an oSEM signal generated using inhomogeneous length scales and the corresponding input Reynolds stresses from a LES of channel flow. The oSEM does not reproduce the target one-point statistics due to violation of the homogeneous length scale requirement. The most significant errors occur near the wall where the streamwise length scales are highly elongated.

Another limitation of the oSEM is the rate of convergence of the generated signal toward the correct input statistics. The design of the oSEM does not guarantee reproduction of input statistics for any signal time period, but a convergence toward the input statistics in time. Although a signal created by the oSEM will eventually converge to the input statistics, the rate of convergence is problem specific. The extent of convergence is not known until after simulation run time.

Finally, the random placement of inhomogeneous eddies can be very inefficient since the required number of eddies for adequate coverage of the inlet plane will be dictated by the smallest eddies. This results in an over-population of larger eddies, increasing the computational cost as the cost of the SEM scales with the number of eddies used to generate the signal.

The limitations above require a compromise in the application of the oSEM. Either a uniform length scale and a limited shape function must be used as inputs to recapture the prescribed Reynolds stresses, which causes an inaccurate distribution of energy at realistic wave numbers, or, a more realistic variation of length scales and shape functions can

be specified for the velocity components (e.g., as a function of distance from a wall), which causes errors in the output Reynolds stresses and thus creates inaccurate levels of turbulent kinetic energy (TKE) in the flow.

2.2. Previous improvements to the SEM

Pamies et al. [15] addresses the homogeneity limit by implementing the SEM in discrete “modes” at select heights above the wall that represent canonical regions of the boundary layer. Each mode uses distinct convective velocities, shape functions, and locally homogeneous length scales so that, individually, each SEM mode satisfies the homogeneous length scale requirement. They also include the effects of variable coherent structures, such as quasi-streamwise vortices in the buffer layer and hairpin vortices in the log layer, by varying the shape function associated with each mode. Together, the modes approximate the inhomogeneity of wall-bounded flows. This method, however, adds considerable complexity with the implementation of multiple SEM instances and the handling of the boundaries between the modes. Additionally, there is a practical limit of a finite number of modes.

Skillen [16] proposes an alternate normalization to Eq. (4) to remove the requirement of random eddy placement. Using this normalization, one is free to generate eddies of arbitrary length scales and still recapture the input Reynolds stress tensor in the statistical limit. This provides a new way to reduce the cost of the SEM by using a more physically consistent distribution of eddies of varying size in the flow. However, the alternate normalization of [16] relies on imprecisely defined time scales estimated prior to the simulation time. The effect these time scales have on the convergence rate is unknown to the user until the simulation is complete. Thus, the rate of convergence to the correct statistics may be too slow for reasonable simulation times.

Luo et al. [17] implements a similar approach to Pamies et al. [15], but with overlapping SEM eddy volumes. These “multi-domains” are specified with judiciously selected length scales to obtain a desired energy spectrum at different heights above the wall. Termed multiscale-SEM, the approach utilizes a simplified Reynolds stress tensor and convects eddies at the local mean velocity. As eddies exit a specified domain, new eddies are regenerated in the same domain, the height of which is related to the local mean velocity to avoid accumulation of eddies in slower regions of the flow. To accomplish this, however, the method uses restrictive closed-form expressions for the length scales and adds complexity relative to the oSEM by requiring multiple simultaneous implementations to generate a signal.

With different objectives in mind, Poletto et al. [18] developed a SEM that attempts to enforce a divergence free approximation for purely incompressible flow. The motivation for divergence free inflow is primarily due to issues related to incompressible flow solvers, where non-solenoidal inflow fluctuations can cause numerical difficulties when iterating on pressure and velocity. Since the signal being generated only exists in two spatial dimensions plus the temporal dimension, it is not possible to enforce the divergence free condition exactly. However, the inflow signal can be made closer to solenoidal to reduce small spurious pressure oscillations near the inlet. The method applied in [18] shows significant improvements in convergence of incompressible flow solvers. However, the approach is still subject to the limitations associated with the oSEM and the improvements outlined above. Note also that for compressible flow solvers, the solenoidal nature of the inflow signal is of no consequence. Any of the modifications to the oSEM outlined above and those proposed in the current paper can be modified using approaches such as those proposed in [18] and will be impacted similarly by the additional approximations.

While the above improvements have successfully extended the capability of the oSEM, they also add additional trade-offs in terms of accuracy, cost, complexity, and the types of approximations required. This introduces new restrictions while eliminating others. The goal of the proposed method is to eliminate as many restrictions to the method as possible while maintaining the simplicity of the original method and simultaneously minimizing the computational cost.

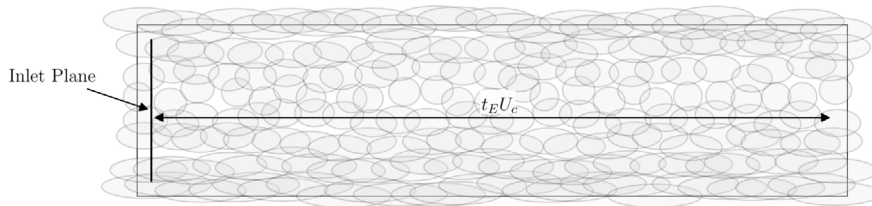


Fig. 3. Extruded-eddy-volume, populated with current and future synthetic eddies.

3. An ensemble approach to the SEM

Given the current trade-offs in terms of accuracy and cost, an alternative implementation of the SEM is proposed, which is denoted as the ESEM. To date, all SEM implementations generate the inflow signal as a simulation progresses. Thus, the eddy volume is only populated with eddies that contribute to the signal at the current instant in time, as illustrated in Fig. 1. Instead, one can extend the eddy volume forward in time to include “future” eddies. This requires determining an ensemble signal time, t_E , which represents how far into the simulation future the inlet boundary condition is generated. Once an ensemble signal time is selected, an “extruded-eddy-volume” is generated with a streamwise length of $x_E = t_E U_c$, where U_c is the bulk convective velocity of the flow. The volume is then populated with both current and future eddies, as illustrated in Fig. 3.

Once the extruded-eddy-volume is populated with eddies, the unnormalized signal is generated via Eq. (1) for the entire duration of the ensemble signal time. The signal is generated at selected integration time steps corresponding to the simulation. The generated signal can be stored and applied as the simulation progresses. Note that the ensemble signal time, t_E , is arbitrary and flexible. It can be as long as the duration of a simulation or as short as an ensemble window that provides adequate statistical separation. In the former case, the entire inlet signal is generated before time integration begins. In the latter case, only an ensemble window of the inlet signal is generated and either repeated periodically over the interval t_E , or alternatively a new extruded-eddy-volume can be generated and populated at the end of an ensemble time interval.

The major advantage of the proposed approach is the generation of the entire un-normalized signal *before* normalization instead of approximately normalizing as the signal is being generated as in Eq. (4). Having access to the entire un-normalized signal enables explicit enforcement of zero mean, $u_i^{**} = u_i^* - \langle u_i^* \rangle$, and unit variance, $u_i^{***} = u_i^{**}/\sqrt{\langle u_i^{**2} \rangle}$, on u_i^* . Thus, an exact normalization is applied over the ensemble signal time instead of the approximate normalization of Eq. (4).

After normalization, the Cholesky decomposition is used to produce the final signal,

$$u_i = a_{ij} u_i^{***}. \quad (7)$$

With the zero mean and unit variance properties strictly enforced, the application of the Cholesky decomposition in Eq. (5) reproduce the desired one point statistics nearly exactly. Note that the requirement of zero covariance between the u_i^* components for $i \neq j$ of the un-normalized signal can also be exactly enforced by a whitening procedure. This aspect is described in more detail in Appendix B. However, the whitening procedure was found to corrupt the spatial coherence in parts of the generated signal. Instead, the ESEM relies on the random prescription of fluctuation signs, $(\epsilon_i)_k$, as in the oSEM.

With the explicit enforcement of zero mean and unit variance, all algorithmic restrictions in the oSEM involving these requirements are lifted, yielding the following advantages:

Flexibility of the ESEM

1. No requirement for random placement of eddies similar to [16].

2. Allows for the convection of eddies with arbitrary velocities.
3. Prescription of arbitrary eddy length scales to account for inhomogeneous turbulence.
4. Utilization of arbitrary shape functions that do not adhere to the normalization of Eq. (2).

Furthermore, there is no convergence rate associated with a signal generated by the ESEM, as the input statistics are reproduced exactly by the modeled signal over a known time frame (t_E). These properties exist without the drawbacks outlined in Section 2.2, as the method maintains the simplicity of the oSEM. The cost of this flexibility is the need to compute and store the greater number of eddies in the extruded-eddy-volume. Section 4 describes means of reducing this cost. Compute memory and cost estimates, along with other implementation details, are in Appendix C.

4. Advantages of the ESEM

The ESEM formulation guarantees accurate reproduction of signal one-point statistics, without the algorithmic requirements of the oSEM. This flexibility provides the option to add physically relevant flow features, and potentially reduces the cost of computing the signal. This section highlights three examples of utilizing the flexibility of the ESEM by the use of: inhomogeneous length scales, improved eddy placement, and improved shape functions presented in 4.1 – 4.3, respectively. These examples are not inherent to the ESEM, but simply leverage the freedom afforded by the method. Comparisons of generated signal costs and quality for methods using the ESEM and oSEM are presented in 4.4.

4.1. Inhomogeneous length scale prescription

With the ESEM, one is free to vary prescribed eddy length scales as a function of height above the wall while maintaining accurate signal statistics. This allows for targeting the inhomogeneous two-point statistics of wall-bounded flow, and thus prescribe a more accurate distribution of energy across all wavenumbers in all regions of the domain. As is the case for all SEM implementations, one must know, or assume, some information about the length scale distribution for any particular set of simulation parameters. This information can come from theory, simulations, experimental measurements, or any logical combination of each since they are an input to the method.

To incorporate inhomogeneity, the target length scales are decomposed into nine components consisting of one length scale in each coordinate direction for each velocity component. The matrix of scales is denoted

$$\sigma_{ij} = \begin{bmatrix} \sigma_{ux} & \sigma_{uy} & \sigma_{uz} \\ \sigma_{vx} & \sigma_{vy} & \sigma_{vz} \\ \sigma_{wx} & \sigma_{wy} & \sigma_{wz} \end{bmatrix}. \quad (8)$$

This application of inhomogeneous length scales is not new and has been suggested in the past by both Jarrin [19] and Luo et al. [17]. However, with the ESEM one is free to assign arbitrary values to the σ_{ij} components throughout the domain and still recover the target one-point statistics since the zero mean and unit variance enforcement does not depend on the length scale prescription.

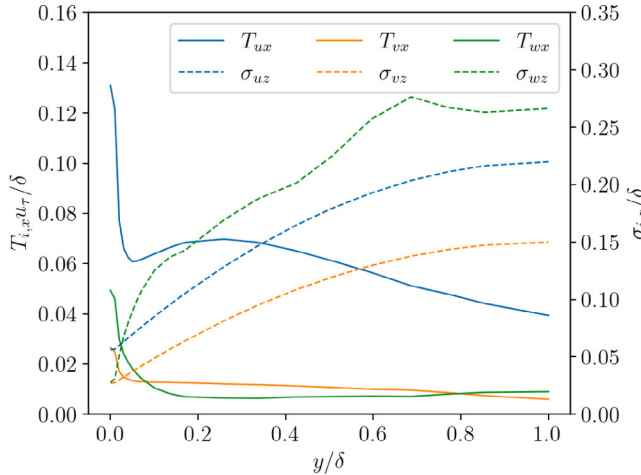


Fig. 4. Length and time scales extracted from a previous LES of fully-developed turbulent channel flow as a function of height above the wall. These data are used as the target input for the SEM tests.

In the current work, the length scale distributions in Eq. (8) are approximated by the profiles shown in Fig. 4. These values were computed from the correlation tensor extracted from a previous LES of fully-developed turbulent channel flow. Note that the streamwise components in Fig. 4 are time scales. The streamwise time scales of Fig. 4 are converted to appropriate length scales based on the eddy convective velocity, $\sigma_{ix} = T_{ix} U_c$, where terms T_{ix} are the corresponding integral time scales associated with the streamwise components in Eq. (8). These length scales approximate the two-point statistics of the correlation tensor, and related energy spectra. While precise reproduction of the correlation tensor is not guaranteed, the goal is to generate signals that consist of the fluctuation components of the prescribed length scales. Although there may be uncertainty in the prescribed input to ESEM, the output signal remains coherent and will reproduce the input statistics without introducing additional errors.

4.2. Improved eddy placement

The use of the extruded-eddy-volume in the ESEM increases the number of eddies that must be stored and computed by a significant factor. To alleviate this additional cost, the ESEM allows for more efficient means of computing the number and placement of eddies given random eddy placement is not a requirement. In the oSEM formulation, the number of eddies distributed within the eddy volume is straightforward: $N = C_{\text{eddy}} V_B / \sigma^3$, where C_{eddy} is a scale factor to ensure coverage at every point on the inlet plane. Since the eddy density is uniform for the oSEM, the accuracy of the oSEM signal statistics do not strongly depend on the number of eddies. However, inhomogeneous length scales make the eddy volume in Eq. (4) ill-defined. Additionally, if nine component length scales are used as described in Section 4.1, each eddy has three separate volumes that must be considered: one for each velocity component; i.e., $V_i = \sigma_{ix} \sigma_{iy} \sigma_{iz}$. A conservative method of prescribing the number of eddies with inhomogeneous length scales is $N = C_{\text{eddy}} V_B / \min(V_i)$, where the minimum eddy volume provides a reference for the number of eddies placed. For a purely random placement of eddies, one must avoid populating small eddies too sparsely, which could result in regions of the inlet plane with zero eddies contributing to the fluctuation signal. However, randomly populating the eddy volume results in excessive generation of larger eddies. The computational cost of the SEM scales with the number of eddies, therefore random placement of inhomogeneous eddies is inefficient.

A more efficient way of generating eddies is to distribute more eddies in regions where they are smaller and reduce the number of

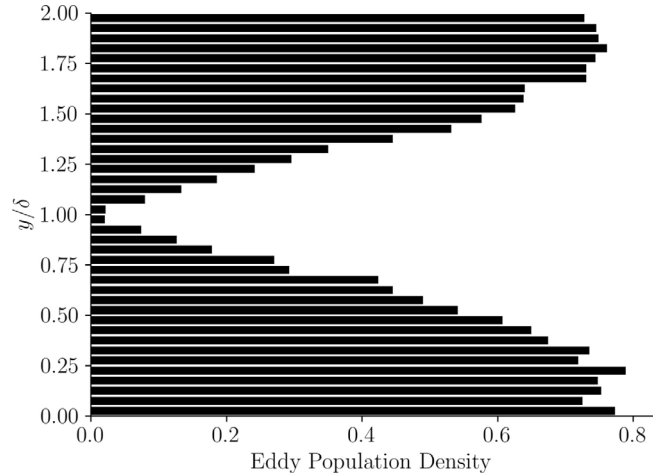


Fig. 5. Histogram of eddy placement given the PDF placement of Eq. (9).

eddies placed in regions where they are larger, such as the core region in a channel flow. This approach can be generalized by constructing a probability density function (PDF) with a linear relationship between the eddy volume as a function of height above the wall, and the probability an eddy exists at this height. Such a PDF would be of the form

$$PDF(y) = \frac{1}{\int \left[\frac{-V(y) + \max(V(y))}{\min(V(y))} + 1 \right] dy} \left[\frac{-V(y) + \max(V(y))}{\min(V(y))} + 1 \right], \quad (9)$$

where $\min/\max(V(y))$ is the maximum/minimum eddy volume as a function of height above the wall. One can evaluate the integral in Eq. (9) numerically. As for the number of eddies placed, one can use the expected eddy volume from Eq. (9) via the relation

$$N = C_{\text{eddy}} \frac{V_B}{E[PDF(y)]}. \quad (10)$$

The scaling parameter, C_{eddy} , adjusts the coverage. Eq. (9) is then used to populate the extruded-eddy-volume with N eddies.

A histogram of eddy placement in a channel flow using this PDF placement method is shown in Fig. 5. The result is an eddy distribution that favors placement in regions of smaller eddies and allows for complete eddy coverage of the inlet plane with a minimal number eddies compared to a purely random placement of eddies. For the example shown here, which uses the length scale specification of Fig. 4, the difference in number of eddies required for complete coverage is an order of magnitude less for the PDF placement method compared to a random placement of eddies.

4.3. Improved shape functions

The final proposed leveraging of the flexibility offered by the ESEM involves the shape function used to characterize the influence of the synthetic eddies. The oSEM requires compact support for a shape function over the length scale of the eddy as well as the normalization of Eq. (2). Since the tent function of Eq. 1 is a common choice, we will focus on the consequences of using the tent function to prescribe inhomogeneous length scales. Fig. 6 shows a one-dimensional tent function with inhomogeneous length scale specifications for each velocity component. The difference between the three component length scales causes disparate eddy volumes. In the example of Fig. 6, the u component has a much larger extent of influence compared to the v or w components. As mentioned previously, the smallest length scale (w in the case of Fig. 6) will dictate the number of eddies generated to ensure all components have non-zero eddies throughout the signal.

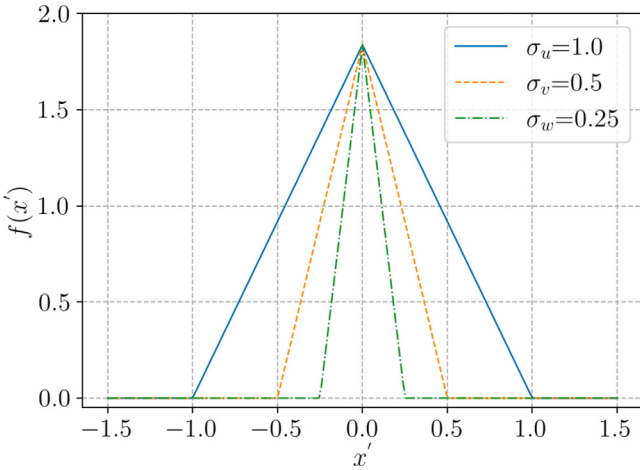


Fig. 6. Inhomogeneous tent shape function with three unique length scales.

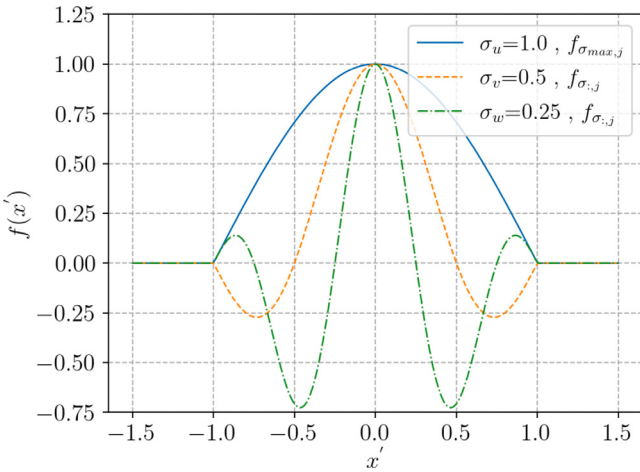


Fig. 7. Modified Inhomogeneous shape function.

An improved shape function unifies the treatment of synthetic eddies with inhomogeneous length scales, as shown in Fig. 7. Instead of an eddy defined by three distinct volumes of influence, a single volume of influence defines an eddy while encapsulating all nine length scales, σ_{ij} , prescribed in Eq. (8). To achieve this goal, $\sigma_{\max,j}$ is defined as the largest length scale in a coordinate direction (column-wise in Eq. (8)) and $\sigma_{:,j}$ as the two shorter length scales in the coordinate direction. Further, let $f_{\sigma_{\max,j}}$ and $f_{\sigma_{:,j}}$ be the shape functions for the largest and shorter two length scales (column-wise in Eq. (8)), respectively. Then the eddy shape function is defined as

$$\begin{aligned} f_{\sigma_{\max,j}}(x') &= \begin{cases} \cos\left(\frac{\pi x'}{2\sigma_{\max,j}}\right) & |x'| \leq \sigma_{\max,j} \\ 0 & |x'| > \sigma_{\max,j} \end{cases} \\ f_{\sigma_{:,j}}(x') &= \begin{cases} f_{\sigma_{\max,j}}(x') \cos\left(\frac{\pi x'}{2\sigma_{:,j}}\right) & |x'| \leq \sigma_{\max,j} \\ 0 & |x'| > \sigma_{\max,j} \end{cases} \end{aligned} \quad (11)$$

This unified shape function is then substituted into the un-normalized signal of Eq. (1),

$$u_i^*(x, y, z) = \sum_{k=1}^N (\epsilon_i)_k [f_{i,x}(x - x_k) f_{i,y}(y - y_k) f_{i,z}(z - z_k)]. \quad (12)$$

Fig. 7 shows the results of this shape function for the same length scales used in Fig. 6. Resulting eddies have individual volumes defined

Table 1
Summary of test channel flow.

Channel height	2δ
Channel width	3δ
Re_τ	587
u_τ [m/s]	1.411
U_c [m/s]	30.0
Total signal time [s]	$10\delta/u_\tau$
Ensemble signal time [s]	$10\delta/u_\tau$
Time steps	4000

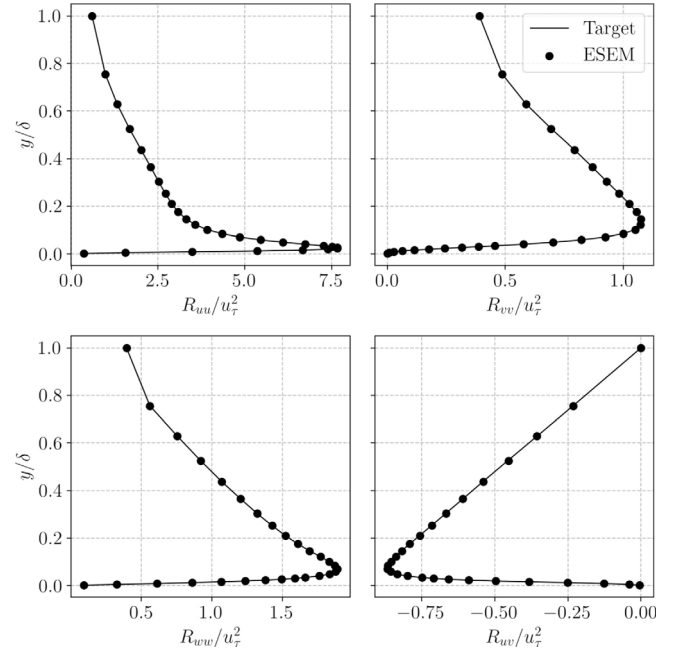


Fig. 8. Statistics of the Ensemble SEM with inhomogeneous length scale specification.

by the largest length scale in each coordinate direction. However, respective eddy components still contribute to each signal component with the desired length scales and spatial frequency. The number of eddies required to maintain eddy coverage over the domain reduces by another order of magnitude for the length scales of Fig. 4 beyond the PDF placement method described in Section 4.2 as each component has the same eddy volume.

4.4. Generated signal cost and accuracy

In this section, turbulent inflow signals for a canonical channel flow on an inlet plane discretized for LES resolution are used to demonstrate the ESEM signal quality. The geometry and bulk features of the channel flow are given in Table 1. The SEM requires three inputs: target one-point statistics for the generated signals, a shape function, and length scales for the synthetic eddies. The target one-point statistics used here are from the DNS data of Moser [20]. Length scales are again taken from Fig. 4 since they correspond to the conditions in [20]. The shape function used is the unified shape function described in Section 4.3. To further emphasize the ESEM's ability to reproduce target length scales, a second signal derived from the length scales of Pamies et al. [15] is generated.

Fig. 8 shows the statistics of the ESEM using inhomogeneous length scales, the PDF placement method of Section 4.2, and the unified shape function of Section 4.3. The explicit normalization of the ESEM allows it to reproduce the input statistics exactly as expected. To assess how well the ESEM captures the input length scales, Fig. 9 shows computed length scales from the ESEM signal compared to the input length scales. For the ESEM signal, the lag distance at which the

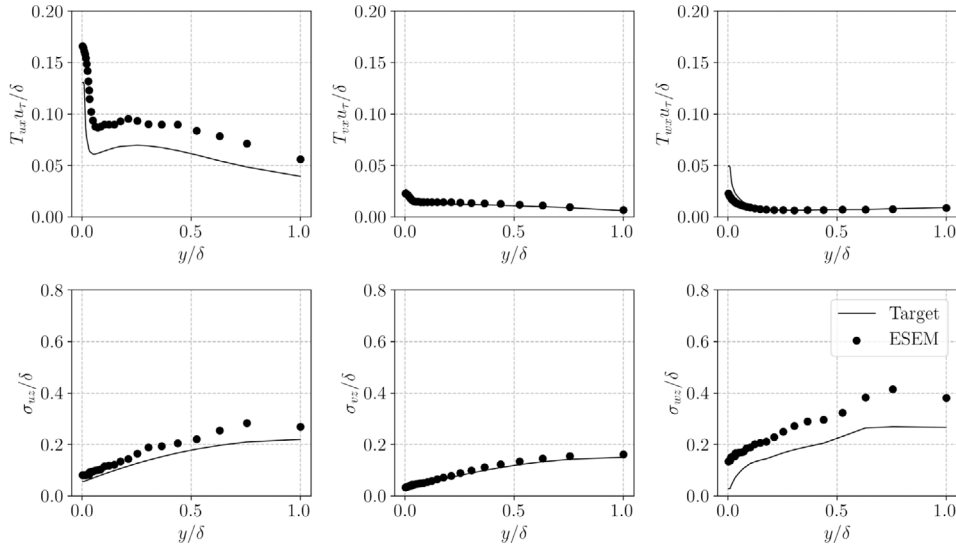


Fig. 9. Length scale comparison from autocorrelation calculations of the ESEM compared to the target length scales generated from LES data.

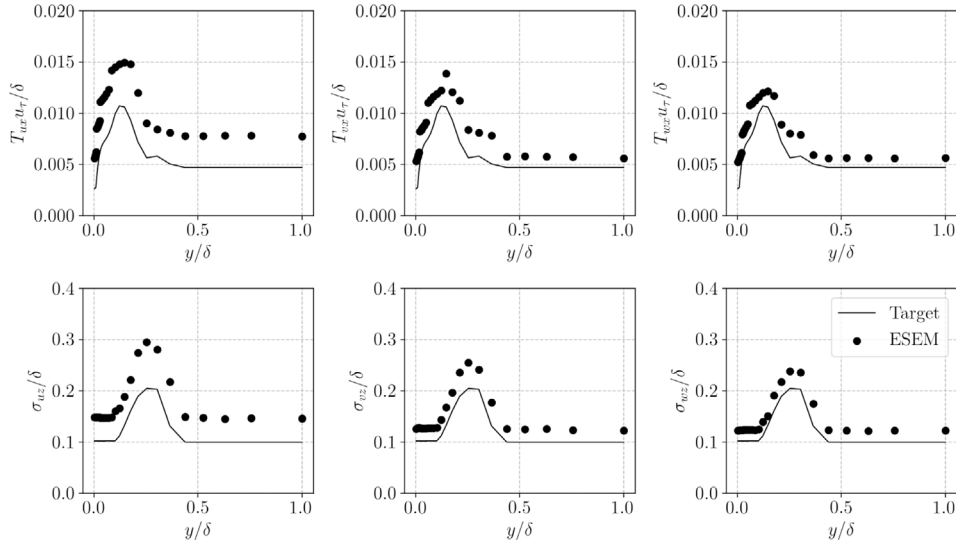


Fig. 10. Length scale comparison from autocorrelation calculations of the ESEM compared to target length scales derived in Pamies et al. [15].

normalized autocorrelation function drops to 0.2 defines the length scale, as suggested by Keating et al. [21]. The computed length scales targeting the Pamies [15] length scales are shown in Fig. 10. The precise reproduction of length scales is not guaranteed by the method. The effect of the shape function and overlapping eddies on the resulting length scales is unknown. Despite this, in both cases the ESEM generates signals that match the trends of the input length scales at all heights above the wall. The reproduction of the target length scales is critical, as it verifies the spatial and temporal coherence is intact (even after application of the Cholesky decomposition) and the accurate targeting of an autocorrelation.

Results comparing the required number of eddies for inlet plane coverage and the related error in second-order statistics from six variations of SEM signals are listed in Table 2. For the oSEM calculation, N in Table 1 is the total eddies generated over the duration of the calculation. For the ESEM calculation, the ensemble time is the entire signal time. The cost of the SEM scales directly with the number of eddies, i.e. fewer required eddies results in less computational costs.

The error in statistics is the average over the wall normal direction as given by

$$e_{ij} = \frac{1}{\delta} \int_0^\delta \left| \frac{R_{ij,\text{Target}} - R_{ij,\text{SEM}}}{R_{ij,\text{Target}}} \right| dy. \quad (13)$$

The signal generated with the length scales from Pamies et al. [15] requires a much larger number of eddies than the signal generated using the LES-derived length scales. The Pamies length scales are nearly an order of magnitude smaller than the LES-derived length scales requiring more eddies to maintain inlet coverage. For more details on the computational costs of the ESEM, see algorithmic details in Appendix C.

The ESEM reproduces the input one-point statistics accurately at a fraction of the required synthetic eddies, while also capturing the inhomogeneity of the input length scales. As mentioned earlier, precise reproduction of input length scales is not guaranteed by the method. The consequences of the eddy population, population method, shape function, etc. on the reproduction of the input length scales is a subject of future work.

Table 2

Performance of various SEM signal generation methods.

Norm	σ_{ij}	Population	Shape	N	e_{uu}	e_{vv}	e_{uw}	e_{uv}
oSEM	$\sigma = 0.15\delta$	Random	Tent	0.38 M	<1%	<1%	<1%	<1%
oSEM	Fig. 4 ^a	Random	Tent	3.64 M	27%	31%	32%	19%
oSEM	Fig. 4 ^a	PDF ^a	Tent	0.79 M	82%	84%	82%	60%
ESEM	Fig. 4	PDF	Tent	0.79 M	<1%	<1%	<1%	<1%
ESEM	Fig. 4	PDF	Unified	0.24 M	<1%	<1%	<1%	<1%
ESEM	Pamies [15]	PDF	Unified	1.2 M	<1%	<1%	<1%	<1%

^aViolates oSEM formulation.**Table 3**

Parameters of LES test case.

Re_τ	Re_c	L_x	L_y	L_z	n_x	n_y	n_z	Δx^+	Δy^+_{\min}	Δy^+_{\max}	Δz^+
587	12,485	12δ	2δ	6δ	469	156	234	15	0.5	15	15

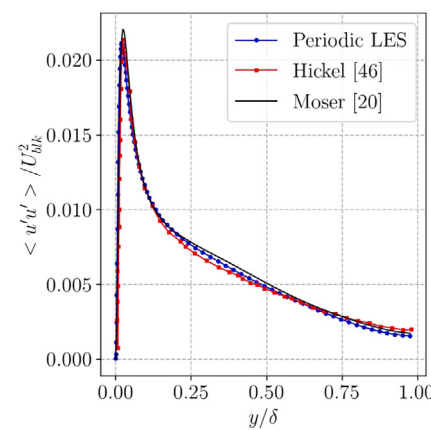
5. LES channel flow results

In this section, results from a reference streamwise-periodic fully-developed turbulent channel flow are compared to various implementations of the SEM used to generate inflow boundary conditions at the same conditions. Key parameters associated with the reference case are given in Table 3. The streamwise-periodic flow is driven using a time-dependent body force to enforce a constant target mass flow rate. Corresponding cases using different SEM approaches as inlet conditions, including the ESEM, are then performed to investigate the relative performance and accuracy of the different methods.

5.1. Numerical approach

Simulations of the reference turbulent channel flow were performed using the RAPTOR code framework developed by Oefelein, which is a massively-parallel combined DNS and LES solver that has been optimized to meet the strict algorithmic requirements imposed by the LES formalism. In the most general case, the theoretical framework solves the fully-coupled compressible conservation equations of mass, momentum, total-energy, and species for a multicomponent reacting flow system. It is designed to handle high-Reynolds-number, high-pressure, multiphase flows over a wide Mach operating range (including the incompressible limit). Details related to the baseline formulation and models are given by Oefelein [22]. Details related to the algorithmic design and massively-parallel programming model can be found in [23, 24]. Selected case studies are described in Refs. [25–45]. The following provides a summary of the main algorithmic features of the code.

The temporal integration scheme employs an all-Mach-number formulation using dual-time stepping with generalized preconditioning. The approach is up to fourth-order accurate in time and provides a fully-implicit solution using a fully-explicit (highly-scalable) multistage scheme. Preconditioning is applied on an inner pseudo-time loop and coupled to local time stepping techniques to minimize convective, diffusive, geometric, and source term stiffness in an optimal manner. The formulation is A-stable, which conceptually allows one to set the physical time step based solely on accuracy considerations. This attribute typically provides a 1 to 2 order of magnitude increase in the allowable integration time step compared to conventional compressible flow solvers, especially in low Mach number incompressible flow regimes. The spatial scheme is designed using non-dissipative, discretely-conservative, staggered, finite-volume differencing. The differencing methodology has been specifically designed for LES. In particular, the staggered-grid formulation fulfills two key accuracy requirements. First, it is spatially non-dissipative, which eliminates numerical contamination of the sub-filter models due to artificial dissipation. Second, it provides discrete conservation of mass, momentum, energy, and species, which eliminates the artificial build up of energy at the high wavenumbers.

Fig. 11. $\langle u'u' \rangle / U_{blk}^2$ for periodic LES case compared to LES of [46] and DNS of [20].

For the reference channel-flow LES performed here, the RAPTOR code is used to solve the Navier-Stokes equations for inert air assuming it is a calorically perfect gas. The “mixed” dynamic Smagorinsky model is used to approximate the subgrid stresses with test filtering performed at twice the local filter width. In contrast to what is typically referred to as simply the dynamic Smagorinsky model, the “mixed” model includes a scale-similarity model that facilitates inclusion of the “Leonard-stresses” and “cross-term-stresses” [47,48]. This is accomplished based on the assumption that certain multiscale flow characteristics are the same between resolved-scale and subgrid quantities in the vicinity of the cutoff scale. Including the scale-similarity model has been shown to provide the correct energy dissipation rate to the large scales. See [22] for additional details on the models used. The physical time step used for the calculations is $0.003\delta/U_c$, where δ is the channel half-height and U_c is the bulk flow velocity. Fig. 11 shows the streamwise Reynolds stress from this simulation compared to the DNS results from Moser et al. [20] and LES results from Adams and Hickel [46]. Note that the Reynolds stresses of both the streamwise periodic case performed here and Adams and Hickel [46] are in good agreement with the DNS results. Thus, these results were used as benchmark input data for the evaluations that follow. All of the SEM cases presented below use the same grid and flow conditions that were used for the reference periodic case.

5.2. Qualitative characteristics of ESEM inflow signals

This section presents the qualitative characteristics of an inflow signal generated using the ESEM at conditions identical to the reference test case described above. The mean velocity profile and Reynolds stress tensor used as input to create the signal are taken from the DNS results of Moser et al. [20]. The integral scales, σ_{ij} , associated with Eq. (8) are taken from the reference periodic simulation results. The ESEM signal was generated for a total time of $60\delta/U_c$.

Contours of the instantaneous streamwise velocity of the reference LES case using periodic inflow conditions and an LES using the ESEM to generate the inflow conditions are shown in Fig. 12. All four figures are plotted in an identical manner. The inlet plane, shown in Fig. 12, shows the inhomogeneous prescription of small (in the wall-normal and spanwise direction) eddies near the wall and larger eddies toward the channel center. By 4δ , the ESEM field is similar in structure and magnitude to the periodic LES results, as turbulent mixing has occurred and the synthetic near-wall eddies have given rise to “real” turbulence. By 11δ , the ESEM flow has progressed further toward the periodic case, though the channel center lacks some of the large positive streamwise velocity contours of the periodic case. Additionally, the ESEM flow features fewer deep incursions of the high momentum fluid into the buffer layer.

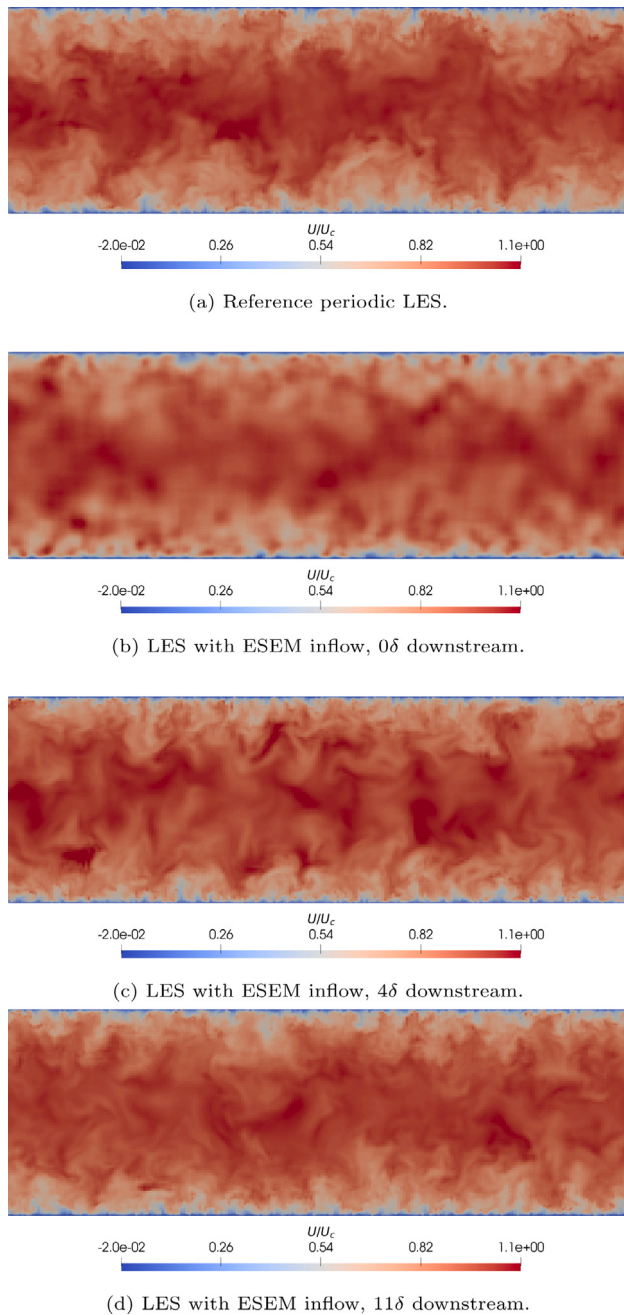


Fig. 12. Comparison of the instantaneous streamwise velocity contours between the reference LES using periodic inflow conditions and LES using the ESEM to generate the inflow conditions.

Fig. 13 shows the development of the near wall vortices visualized with iso-surfaces of Q-criterion for the ESEM inflow case compared to the reference periodic case. The presence of small vortices near the inlet for the ESEM inflow case are indicative of a qualitatively accurate inflow length scale prescription. By 6δ downstream, these vortices have formed to cover an area quantitatively similar to the reference case. As noted by [15], these small vortices are instrumental for establishing an accurate representation of the skin friction coefficient since they directly influence the near wall velocity field.

The larger vortical structures of the periodic LES and LES with ESEM inflow are shown in **Fig. 14**. These larger structural elements contribute to the development of the Reynolds stresses in the channel center.

Fig. 15 shows the spatial development of the root-mean-square (rms) velocities and Reynolds shear stress for LES with ESEM inflow

compared to the streamwise periodic case. The initial wall-normal and spanwise rms velocities decrease from the target values, especially in the channel center. However, the magnitudes increase toward the reference case values as the larger eddies begin to take on more realistic shapes from their initial approximations.

5.3. Comparison between SEM inflow approaches

In this section, the quantitative performance of three SEM inflow approaches for LES are compared. First, the oSEM is applied using a homogeneous length scale of $\sigma = 0.15\delta$, as was used previously. Second, the approach described as oSEM-inh is applied using the same procedure as the oSEM, but using the inhomogeneous length scale distributions given in **Fig. 4**. Finally, the ESEM approach is applied using inhomogeneous length scales and PDF eddy placement, as described in Section 4. Each of these implementations uses the same mean velocity profile, Reynolds stress profiles, length scale distributions (with the exception of the oSEM), and convective velocity as input. The eddy coverage parameter, C_{eddy} , is 1.5.

The tent shape function is used for all three cases. Initial transients in the calculations are allowed to propagate for a time of $24\delta/U_c$ before statistics are collected. Once the initial transients wash out of the domain, data for the statistics are collected over a period of $36\delta/U_c$ at a sampling rate of every 10 time steps at 12 slices normal to the streamwise direction. Results are averaged across the span and center plane of these slices as well to take advantage of homogeneity and symmetry conditions in the channel.

Fig. 16 shows the error in the skin friction coefficient, C_f , at varying locations downstream of the inlet for all three approaches. This error is calculated as the percent difference relative to the reference periodic LES case at the same axial location. All of the errors tend toward zero with streamwise distance, reaching an error of approximately 1% by the end of the domain. However, both the oSEM and oSEM-inh show larger errors in C_f at the inlet compared to the ESEM. The oSEM approach initially under predicts the error in C_f with a maximum absolute value of 15% at 1δ downstream of the inlet, and comes within 5% at 4δ . Conversely, the oSEM-inh approach initially over predicts the error with a maximum absolute value of 8% at 2δ , but does not drop to less than 5% until 6δ downstream. The ESEM approach exhibits the smallest absolute error. It under predicts C_f by a maximum absolute value of 3.5% at the inlet, then continually drops in the streamwise direction converging to less than 1% at a streamwise location of approximately 4δ .

Further analysis of the error trends shown in **Fig. 16** reveals that the under prediction of C_f for the oSEM case is due to the inaccurate homogeneous length scale prescription in the near wall region of the flow. The sensitivity analysis conducted by Jarrin in [49] shows that when the length scales of the synthetic signal are under predicted or over predicted, the C_f drops an amount proportional to the amount of deviation from the true length scales. **Fig. 16** shows this trend for C_f for the oSEM case, in which the length scales are homogeneous and therefore do not account for longer streamwise near-wall vortices as the inhomogeneous formulations do. The over prediction in C_f for the oSEM-inh case is due to the over prescription of TKE induced by the use of inhomogeneous length scales (see **Fig. 2**) and the related violation of the normalization condition. The latter has also been shown by Jarrin [19]. The oSEM case has a larger maximum C_f error compared to the oSEM-inh case despite its inflow signal's smaller deviations from the target Reynolds stresses (see **Table 2**). This is due to the fact that C_f has a greater sensitivity to underestimations of length scales compared to inaccuracies in the specification of the input Reynolds stresses [19]. Overall, the ESEM displays a smaller variation of C_f throughout the entire domain, and reaches a smaller error earlier in the domain than oSEM or oSEM-inh.

Cumulative errors of the streamwise component of the Reynolds stress tensor and Reynolds shear stress computed using Eq. (13) are

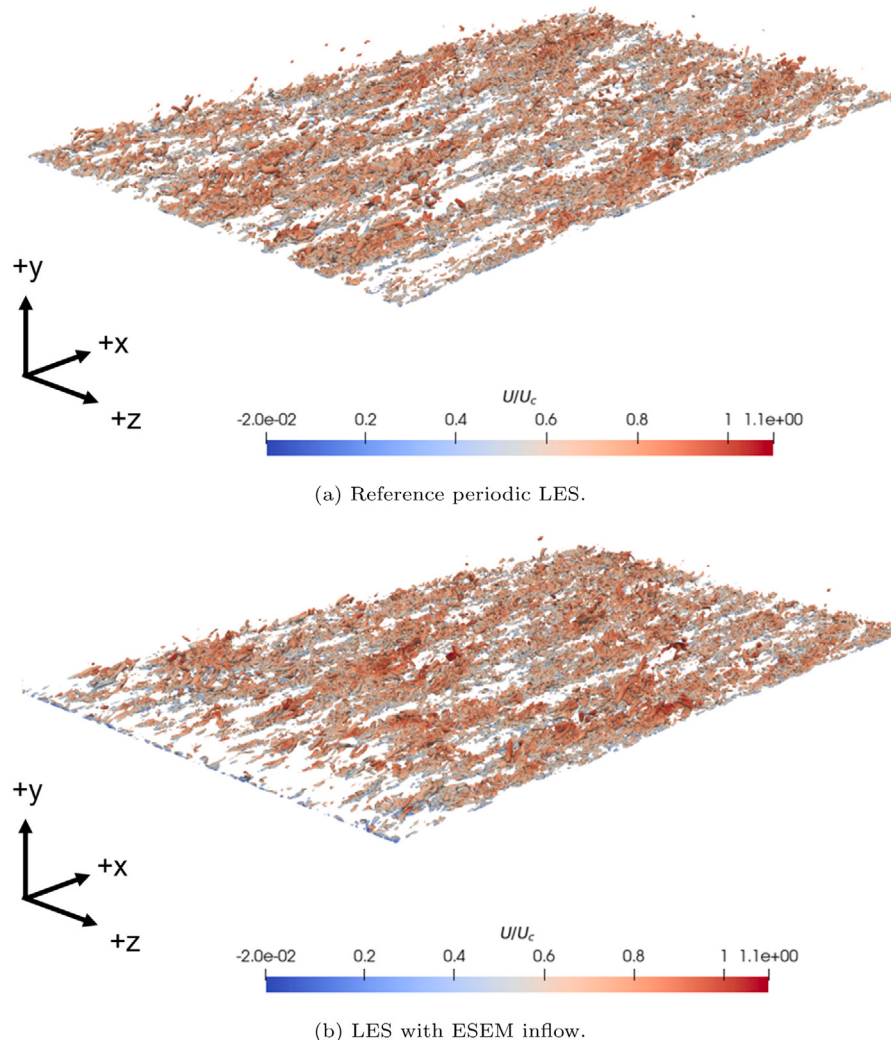


Fig. 13. Development of near wall vortices visualized with iso-surfaces of Q-criterion for the ESEM inflow case compared to the reference periodic case for a Q-criterion threshold of $(-5; 5)$.

shown in Fig. 17. The deviation of R_{uu} for ESEM falls below 10% by 5δ compared to oSEM-inh which reaches 10% at 8δ . The Reynolds shear stress, however, shows a uniformly lower error for the oSEM-inh method throughout the domain. Although the ESEM produces a more accurate R_{ww} for the synthetic signal than oSEM-inh, as shown in Table 2, the wall-normal and spanwise fluctuations experience a sharp drop when introduced into the LES domain, as indicated in Fig. 15. This decrease has been documented in [19]. In addition, it has been observed in [6,19], and [21] that an overestimate of R_{vv} induces the production of R_{uw} more quickly, leading to a faster recovery for oSEM-inh for that component, but at the cost of the errors in R_{vv} and R_{uu} .

Fig. 18 shows the error between the profiles of the ESEM inflow simulation and those of the periodic LES case for the diagonal terms of the Reynolds stress tensor and turbulent kinetic energy. All of the cumulative errors drop below 10% by 7δ with the exception of R_{uw} , which drops to a minimum of 11% at 7δ . The ESEM has been shown to improve upon oSEM-inh in key metrics while requiring fewer eddies and allowing precise matching of the target Reynolds stresses.

6. Conclusion

An Ensemble Synthetic Eddy Method has been presented and demonstrated to provide improved signal accuracy, the option to add

physically relevant flow features, and potentially reduces the cost of computing an artificial turbulent inflow signal. The desired one-point statistics are guaranteed, and the length scales of an input correlation tensor (and subsequent energy spectra) are targeted. These improvements achieve less development length (and related computational time) for the signal to transition to an actual solution of the governing conservation equations after it is imposed and evolves within a computational domain. Major advantages of the method are as follows: (1) The input statistics are reproduced exactly by the modeled signal. (2) It has no requirement for random placement of synthetic eddies. (3) It allows for the convection of eddies with arbitrary velocities. (4) It can incorporate the prescription of arbitrary eddy length scales to account for inhomogeneous turbulence. (5) It can incorporate arbitrary shape functions. Practitioners are free to specify inputs that produce more physically relevant and complex flow features, improve the accuracy of the signal, and reduce the computation cost of generating the signal.

Three examples of leveraging the flexibility of the ESEM were demonstrated: specification of inhomogeneous length scales without loss in accuracy of the generated second-order statistics, a general method of placing eddies and accounting for inhomogeneities in the structure of the synthetic eddies, and the modification of the eddy shape function to provide a unifying structure to the synthetic eddies and avoid the cost associated with disparate eddy component volumes. These improvements provide an adaptable framework for generating high quality turbulent inflow signals.

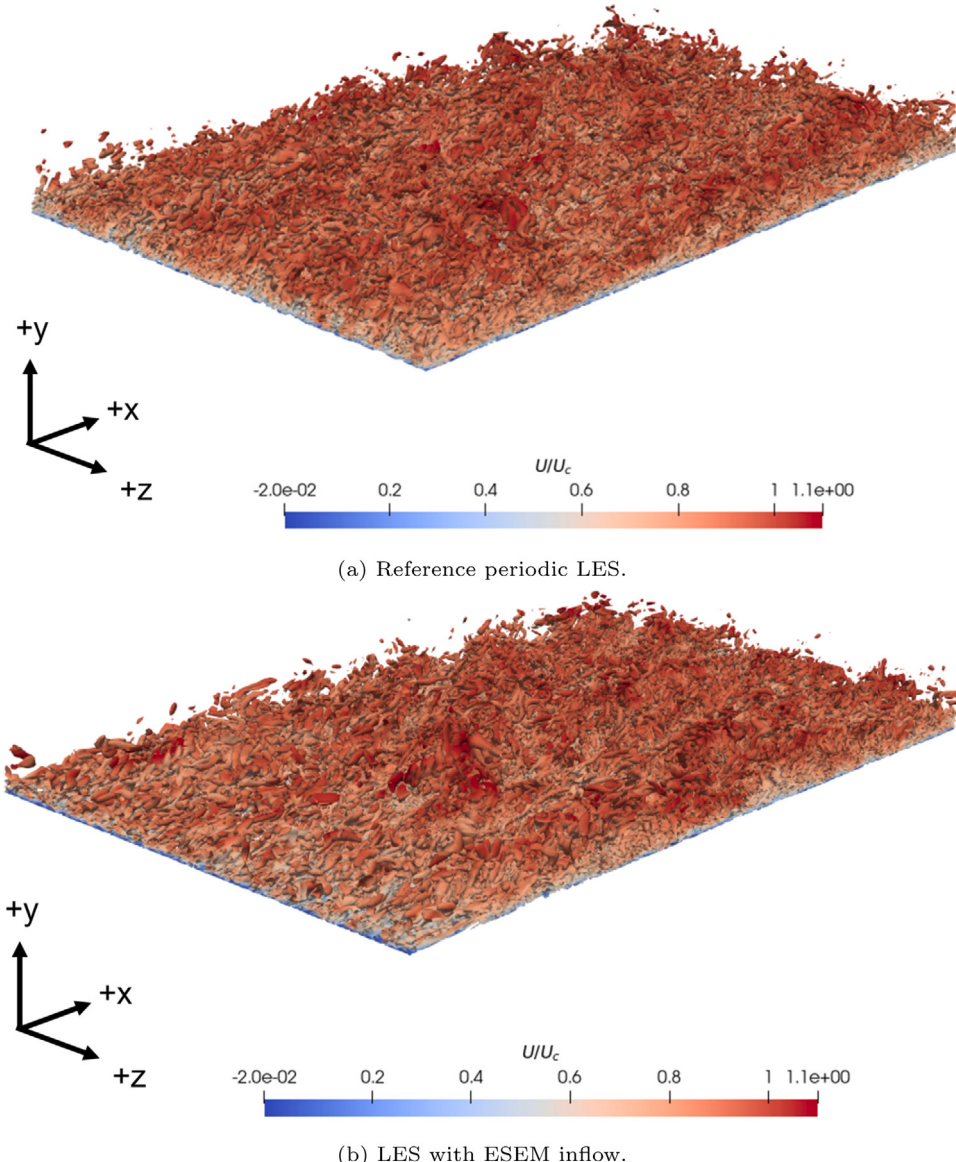


Fig. 14. Large scale structure, Q-criterion (1.0; -1.0).

LES calculations leveraging these improvements show favorable qualitative features compared to a reference periodic LES channel flow as well as quantitative improvement over the original Synthetic Eddy Method in terms of skin friction coefficient and Reynolds stress profiles downstream of the channel inlet. Generating the ensemble signal facilitates the modeling of more complex eddy shapes, more realistic distribution of energy over wavenumbers, and continued improvements in the capability and utility of the SEM approach.

CRediT authorship contribution statement

Kyle A. Schau: Conceptualization, Methodology, Software, Validation, Writing – original draft. **Chelsea Johnson:** Conceptualization, Data curation, Validation, Visualization, Writing – original draft. **Julia Muller:** Conceptualization, Validation, Data curation, Writing – review & editing. **Joseph C. Oefelein:** Funding acquisition, Investigation, Resources, Supervision, Writing – review & editing.

Declaration of competing interest

The authors declare that they have no known competing financial interests or personal relationships that could have appeared to influence the work reported in this paper.

Data availability

Data will be made available on request.

Acknowledgments

The authors gratefully acknowledge the support of the Air Force Office of Scientific Research (AFOSR), United States of America under Federal Award Number FA9550-19-1-0313 with Dr. Chiping Li and Dr. Sarah Popkin as program officers, and the National Aeronautics and Space Administration (NASA), United States of America under Federal Award Number 80NSSC19K1682 with Dr. Robert Baurle and Dr. Tomasz Drozda as technical advisors.

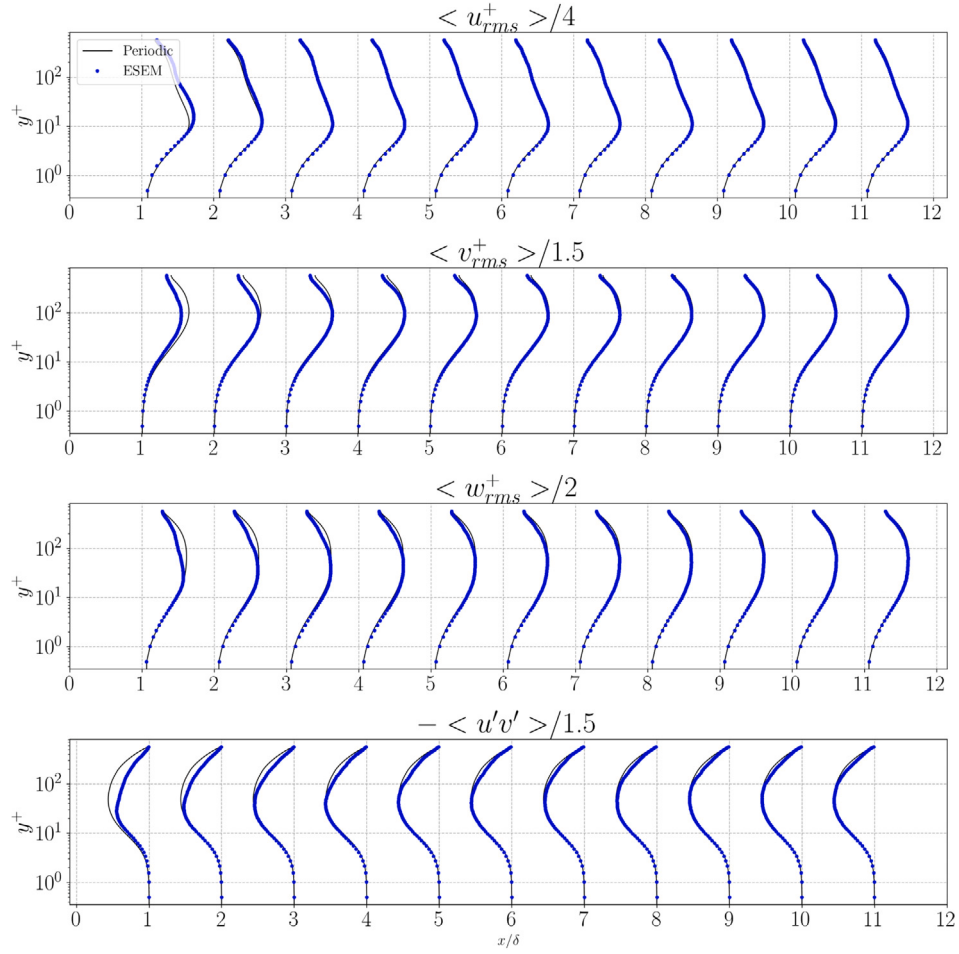


Fig. 15. Spatial development of the rms velocities and Reynolds shear stress for LES with ESEM inflow compared to the streamwise periodic case.

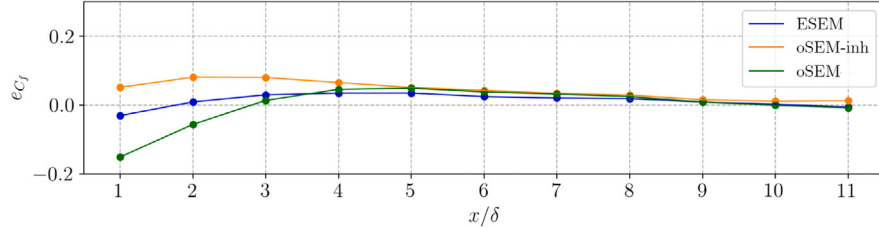


Fig. 16. Evolution of the skin friction coefficient error for the oSEM, oSEM-inh and ESEM inflow cases relative to the reference periodic LES.

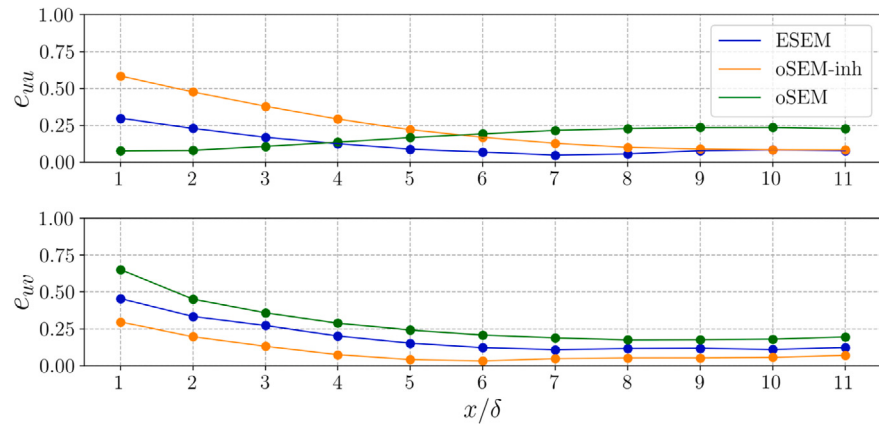


Fig. 17. Cumulative errors of the streamwise component of the Reynolds stress tensor and Reynolds shear stress computed using Eq. (13) for the oSEM, oSEM-inh and ESEM inflow cases relative to the reference periodic LES.

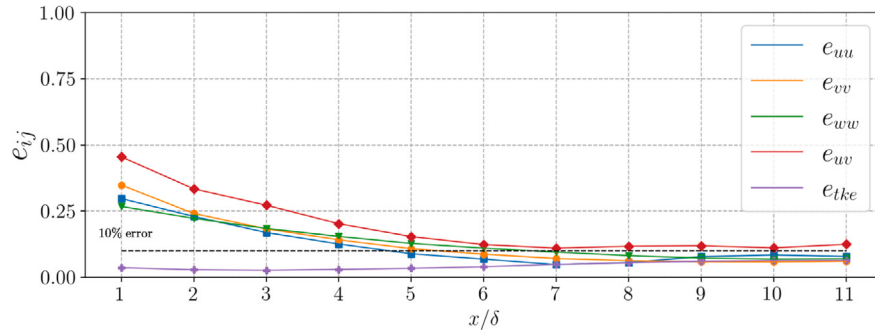


Fig. 18. Cumulative error for Reynolds stress profiles and TKE profile of LES with ESEM inflow.

Appendix A. Impact of Cholesky decomposition

The application of the Cholesky decomposition can negatively affect the un-normalized signal, u_i^* . While providing accurate one-point statistics, the process can corrupt the two-point statistics as mentioned in [50]. The Cholesky decomposition represents a linear combination of the components of u_i^* to produce the final signal, u_i . However, the desired length scale content is already present in the signal u_i^* . Therefore, the operation can corrupt the underlying frequency content of u_i^* for an arbitrary one-point statistic prescription. However, this is only true for two-point statistics with streamwise separation (i.e., the temporal dimension of the inlet signal). Since the Cholesky operator is linear, the two-point statistics with spanwise and wall normal separation remain. Further, for a majority of wall bounded turbulent flows, the negative impact is demonstrably minimal by examining the magnitude of the terms in Eq. (5).

The Cholesky decomposition has no effect on the two-point statistics of the streamwise signal, u_1^* , since it is only scaled by $\sqrt{R_{11}}$. The vertical signal, u_2^* , combines with $R_{21}/a_{11}u_1^*$. For wall bounded flows, the streamwise Reynolds stress, R_{11} , is generally much larger than the off-diagonal component, R_{21} . Thus a_{11} is greater than R_{21} and the operation is primarily a scaling of the original signal u_2^* . Finally, the spanwise signal, u_3^* , is a linear combination of all three un-normalized components. However, if the streamwise-spanwise and wall-normal-spanwise components have no correlation, as is typically the case, the terms R_{31}/a_{11} and $(R_{32} - a_{21}a_{32})/a_{22}$ are effectively zero. Therefore, the spanwise signal, u_3^* , is primarily scaled by a constant factor and retains its frequency content.

These properties allow the spatio-temporal coherence of u_i^* to remain intact after application of the Cholesky decomposition, as shown in Figs. 9 and 10.

Appendix B. Whitening procedure

The un-normalized signal, u_i^* , can be made to contain exactly zero covariance between components using a whitening procedure:

$$u_i^{***} = \lambda_{ij} u_j^{**}, \quad (\text{B.1})$$

where the columns of λ_{ij} are the eigenvectors of the underlying covariance $\text{Cov}(u_i^{**}, u_j^{**})$. These eigenvectors require arrangement such that λ_{ij} is diagonally dominant, and each eigenvector is scaled to ensure all the diagonal elements of λ_{ij} are positive. Utilizing this whitening procedure provides the exact second-order statistics of the input Reynolds stress tensor to within machine precision for every inlet velocity signal.

However, the semi-random nature of u_i^* can create ill conditioned eigen-decomposition. The result is significant shredding of spatial coherence in regions of the inlet plane. Further, with the application of the whitening procedure, the inlet signal reproduces the input statistics with a level of accuracy not present in physical turbulence. Thus, this procedure was omitted in the ESEM, and the random component fluctuation signs ϵ_j produces adequately un-correlated signals, while maintaining the spatial coherence across the inlet plane.

Appendix C. Implementation details

The cost of a SEM signal is proportional to the number of eddies contained within the eddy volume and the resolution of the inlet grid boundary since each eddy must be checked for its contribution to each inlet grid point. Although the ESEM appears more expensive compared to the oSEM due to the use of the extruded-eddy-volume, other benefits offset this potential cost. Here we discuss the implementation details of the signal generated for use in the LES results presented in Section 4.4. The inlet face was comprised of 36,504 grid points, partitioned into 48 blocks (parallel compute regions). Specifying a turbulent signal at a single instance in time for all three velocity components requires just 17.8 KB (kilobytes) of double precision memory per block. The ensemble signal time used was $t_E = 10\delta/U_c$. Using a fixed simulation time step of $0.003\delta/U_c$, the resulting inflow signal represents 56MB of data per block. These memory requirements are trivial in terms of storage on modern consumer grade hardware.

The greater expense to consider is the time and memory to generate the signal. Each synthetic eddy requires roughly 100 bytes of information to represent its position, nine component length scales, and the sign of the fluctuations (ϵ_j in Eq. (4)). As shown in Table 1, the number of required eddies for an ESEM application was $\mathcal{O}(1M)$. Therefore, the total random access memory for computing the signal is roughly 102MB, which is again a trivial quantity for modern compute hardware. The time to generate the signal is implementation dependent, however, timing of the tool used to generate the signals in this work required 1.7 ms per inlet grid point, per signal time instance.

The ESEM can be implemented as part of the CFD simulation code such that the ensemble signal is generated at run time and stored in memory for the duration of the simulation, or as a separate off-line tool in which the signal is pre-calculated, saved in permanent memory, and loaded as an input operation at run time. For this work, the signal was generated as a pre-processing operation. Segments of the signal were then read from the file system, as needed, as the simulation was integrated forward in time. No simulation performance degradation was measured due to this approach.

As a means to speed up calculation of the signal, and to improve implementation flexibility such as allowing for variable time steps, the signal can be represented as cubic splines (or some other appropriate interpolation) between time instances. Sensible calculations using the Nyquist frequency can be made to determine the appropriate temporal spacing between computed signal instances while maintaining frequency content. These time instances can then be used to compute cubic spline polynomials to interpolate at any time between signal time instances. This allows for fewer computed signal time instances and variable simulation time steps. Tests show the statistics of a signal reconstructed from cubic spline polynomials still maintain the desired one-point statistical accuracy.

References

- [1] Wu X. Inflow turbulence generation methods. *Annu Rev Fluid Mech* 2016;49:23–49. <http://dx.doi.org/10.1146/annurev-fluid-010816-060322>, URL www.annualreviews.org.
- [2] Tabor GR, Baba-Ahmadi MH. Inlet conditions for large eddy simulation: A review. *Comput & Fluids* 2009;39:553–67. <http://dx.doi.org/10.1016/j.compfluid.2009.10.007>.
- [3] Lund TS, Wu X, Squires KD. Generation of turbulent inflow data for spatially-developing boundary layer simulations. *J Comput Phys* 1998;140(2):233–58. <http://dx.doi.org/10.1006/jcph.1998.5882>.
- [4] Kraichnan RH. Diffusion by a random velocity field. *Phys Fluids* 2003;13(1):22. <http://dx.doi.org/10.1063/1.1692799>, URL <https://aip.scitation.org/doi/abs/10.1063/1.1692799>.
- [5] Smirnov A, Shi S, Celik I. Random flow generation technique for large Eddy simulations and particle-dynamics modeling . *J Fluids Eng* 2001;123(2):359–71. <http://dx.doi.org/10.1115/1.1369598>.
- [6] Batten P, Goldberg U, Chakravarthy S. Interfacing statistical turbulence closures with large-Eddy simulation. *AIAA J* 2004;42(3):485–92. <http://dx.doi.org/10.2514/1.3496>.
- [7] Patterson JW, Balin R, Jansen KE. Assessing and improving the accuracy of synthetic turbulence generation. *J Fluid Mech* 2020;906:1. <http://dx.doi.org/10.1017/jfm.2020.859>.
- [8] Druault P, Lardeau S, Bonnet J-P, Coiffet F, Delville J, Lamballais E, Largeau J-F, Perret L. Generation of three-dimensional turbulent inlet conditions for large-eddy simulation. *AIAA J* 2004;42(3):447–56. <http://dx.doi.org/10.2514/1.3946>.
- [9] Klein M, Sadiki A, Janicka J. A digital filter based generation of inflow data for spatially developing direct numerical or large eddy simulations. *J Comput Phys* 2003;186(2):652–65. [http://dx.doi.org/10.1016/S0021-9991\(03\)00090-1](http://dx.doi.org/10.1016/S0021-9991(03)00090-1).
- [10] di Mare L, Klein M, Jones WP, Janicka J. Synthetic turbulence inflow conditions for large-eddy simulation. *Phys Fluids* 2006;18(2):025107. <http://dx.doi.org/10.1063/1.2130744>, URL <https://aip.scitation.org/doi/abs/10.1063/1.2130744>.
- [11] Sergent E. Vers une méthodologie de couplage entre la simulation des grandes échelles et les modèles statistiques (Ph.D. thesis), Ecully, Ecole centrale de Lyon; 2002.
- [12] Jarrin N, Benhamadouche S, Laurence D, Prosser R. A synthetic-eddy-method for generating inflow conditions for large-eddy simulations. *Int J Heat Fluid Flow* 2006;27(4):585–93. <http://dx.doi.org/10.1016/j.ijheatfluidflow.2006.02.006>.
- [13] Bendat J, Piersol A. Random data. fourth ed.. Hoboken, NJ: Wiley; 2010.
- [14] Dhamankar NS, Blaisdell GA, Lyrintzis AS. Overview of turbulent inflow boundary conditions for large-Eddy simulations. *AIAA J* 2018;56(4):1317–34. <http://dx.doi.org/10.2514/1.J055528>.
- [15] Pamiès M, Weiss PÉ, Garnier E, Deck S, Sagaut P. Generation of synthetic turbulent inflow data for large eddy simulation of spatially evolving wall-bounded flows. *Phys Fluids* 2009;21(4):45103. <http://dx.doi.org/10.1063/1.3103881>, URL <http://aip.scitation.org/doi/10.1063/1.3103881>.
- [16] Skillen A, Revell A, Craft T. Accuracy and efficiency improvements in synthetic eddy methods. *Int J Heat Fluid Flow* 2016;62:386–94. <http://dx.doi.org/10.1016/j.ijheatfluidflow.2016.09.008>.
- [17] Luo Y, Liu H, Huang Q, Xue H, Lin K. A multi-scale synthetic eddy method for generating inflow data for LES. *Comput & Fluids* 2017;156:103–12. <http://dx.doi.org/10.1016/J.COMPFLUID.2017.06.017>.
- [18] Poletto R, Craft T, Revell A. A new divergence free synthetic eddy method for the reproduction of inlet flow conditions for les. In: Flow, turbulence and combustion, vol. 91. 2013, p. 519–39. <http://dx.doi.org/10.1007/s10494-013-9488-2>.
- [19] Jarrin N. Synthetic inflow boundary conditions for the numerical simulation of turbulence (Ph.D. thesis), The University of Manchester; 2008.
- [20] Moser RD, Kim J, Mansour NN. Direct numerical simulation of turbulent channel flow up to $Re_\tau=590$. *Phys Fluids* 1999;11(4):943–5. <http://dx.doi.org/10.1063/1.869966>, URL <http://aip.scitation.org/doi/10.1063/1.869966>.
- [21] Keating A, Piomelli U, Balaras E, Kaltenbach H-J. A priori and a posteriori tests of inflow conditions for large-eddy simulation. *Phys Fluids* 2004;16(12):4696–712. <http://dx.doi.org/10.1063/1.1811672>.
- [22] Oefelein JC. Large eddy simulation of turbulent combustion processes in propulsion and power systems. *Prog Aerosp Sci* 2006;42(1):2–37.
- [23] Oefelein JC, Sankaran R. Large eddy simulation of reacting flow physics and combustion. In: Straatsma T, Antypas K, Williams T, editors. *Exascale scientific applications: programming approaches for scalability, performance, and portability*. Taylor and Francis Group: CRC Press; 2018, p. 231–56.
- [24] Luo L, Straatsma TP, Suarez LEA, Broer R, Bykov D, D'Azevedo EF, Faraji SS, Gottiparthi KC, de Graaf C, Harris JA, Havenith RWA, Jense HJA, Joubert W, Kathir RK, Larkin J, Li Y-W, Lyakh D, Messer OEB, Norman MR, Oefelein JC, Sankaran R, Tillack AF, Barnes AL, Visscher L, Wells JC, Wibowo M. Pre-exascale accelerated application development: The oak ridge national laboratory summit experience. *IBM J Res Dev* 2020;64(3/4):11:1–21.
- [25] Oefelein JC, Schefer RW, Barlow RW. Toward validation of LES for turbulent combustion. *AIAA J* 2006;44(3):418–33.
- [26] Oefelein JC, Sankaran V, Drozda TG. Large eddy simulation of swirling particle-laden flow in a model axisymmetric combustor. *Proc Combust Inst* 2007;31:2291–9, Distinguished Paper Award, 2007.
- [27] Williams TC, Schefer RW, Oefelein JC, Shaddix CR. Idealized gas turbine combustor for performance research and validation of large eddy simulations. *Rev Sci Instrum* 2007;78(3):035114–1–9.
- [28] Frank JH, Kaiser SA, Oefelein JC. Analysis of scalar mixing dynamics in LES using high-resolution imaging of laser Rayleigh scattering in turbulent non-reacting jets and non-premixed jet flames. *Proc Combust Inst* 2011;33:1373–81.
- [29] Kempf AM, Geurts BJ, Oefelein JC. Error analysis of large Eddy simulation of the turbulent non-premixed sydney bluff-body flame. *Combust Flame* 2011;158:2408–19.
- [30] Oefelein JC. Large eddy simulation of complex thermophysics in advanced propulsion and power systems. In: Proceedings of the 8th U.S. national combustion meeting, invited plenary presentation and paper. 2013, Park City, Utah.
- [31] Oefelein J, Lacaze G, Dahms R, Ruiz A, Misdariis A. Effects of real-fluid thermodynamics on high-pressure fuel injection processes. *SAE Int J Engines* 2014;7(3):1–12.
- [32] Quinlan J, McDaniel J, Drozda T, Lacaze G, Oefelein J. A priori analysis of flamelet-based modeling for a dual-mode scramjet combustor. In: 50th AIAA/ASME/SAE/ASEE Joint propulsion conference and exhibit, paper 2014-3743. 2014, Cleveland, Ohio. Best Paper Award, AIAA High Speed Air Breathing Propulsion Technical Committee, 2015.
- [33] Khalil M, Lacaze G, Oefelein JC, Najm HN. Uncertainty quantification in LES of a turbulent bluff-body stabilized flame. *Proc Combust Inst* 2015;35:1147–56.
- [34] Ruiz AM, Lacaze G, Oefelein JC. Flow topologies and turbulence scales in a jet-in-cross-flow. *Phys Fluids* 2015;27(045101):1–35.
- [35] Ruiz AM, Lacaze G, Oefelein JC, Mari R, Cuendet B, Selle L, Poinsot T. A numerical benchmark for high-Reynolds number supercritical flows with large density gradients. *AIAA J* 2016;54(5):1445–60.
- [36] Oefelein JC. Dynamics of gas-liquid interfaces in high-pressure systems. In: 24th International congress of theoretical and applied mechanics, invited topical lecture and paper. 2016, Montreal, Canada.
- [37] Lacaze G, Vane ZP, Oefelein JC. Large eddy simulation of the HIFIRE direct connect rig SCRAMJET combustor. In: AIAA Science and technology forum and exposition, paper 2017-0142. 2017, Grapevine, Texas.
- [38] Ling J, Ruiz A, Lacaze G, Oefelein JC. Uncertainty analysis and data-driven model advances for a jet-in-crossflow. *J Turbomach* 2017;139(021008):1–9.
- [39] Hakim L, Lacaze G, Khalil M, Sargsyan K, Najm H, Oefelein J. Probabilistic parameter estimation in a 2-step chemical kinetics model for n-dodecane jet autoignition. *Combust Theory Model* 2018;22:446–66.
- [40] Huan X, Safta C, Sargsyan K, Geraci G, Eldred MS, Vane ZP, Lacaze G, Oefelein JC, Najm HN. Global sensitivity analysis and estimation of model error, toward uncertainty quantification in scramjet computations. *AIAA J* 2018;56(3):1170–84.
- [41] Huan X, Safta C, Sargsyan K, Vane ZP, Lacaze G, Oefelein JC, Najm HN. Compressive sensing with cross-validation and stop-sampling for sparse polynomial chaos expansions. *SIAM/ASA J Uncert Quant* 2018;6(2):907–36.
- [42] Tsilifis P, Huan X, Safta C, Sargsyan K, Lacaze G, Oefelein JC, Najm HN, Ghosh RG. Compressive sensing adaptation for polynomial chaos expansions. *J Comput Phys* 2019;380:29–47.
- [43] Lacaze G, Schmitt T, Ruiz R, Oefelein JC. Comparison of energy-, pressure-, and enthalpy-based approaches for modeling supercritical flows. *Comput & Fluids* 2019;181:35–56.
- [44] Soize C, Ghosh RG, Safta C, Huan X, Vane Z, Oefelein J, Lacaze G, Najm H, Tang Q, Chen X. Entropy-based closure for probabilistic learning on manifolds. *J Comput Phys* 2019;388:518–33.
- [45] Oefelein JC, Lacaze G. Large Eddy simulation of liquid injection and combustion processes in high pressure systems. In: Bellan J, editor. *High pressure flows for propulsion applications. Progress in astronautics and aeronautics*, vol. 260. Reston, Virginia: American Institute of Aeronautics and Astronautics; 2020, p. 679–729.
- [46] Hockel S, Adams N. On implicit subgrid-scale modeling in wall-bounded flows. *Phys Fluids* 2007;19(10):105106.
- [47] Bardina J, Ferziger JH, Reynolds WC. Improved subgrid scale models based on large eddy simulation of homogeneous, incompressible, turbulent flows. *Tech. Rep TF-19*, Department of Mechanical Engineering, Stanford, California: Stanford University; 1983.
- [48] Speziale CG. Galilean invariance of subgrid-scale stress models in the large Eddy simulation of turbulence. *J Fluid Mech* 1985;156:55–62.
- [49] Jarrin N. Synthetic inflow boundary conditions for the numerical simulation of turbulence (Ph.D. thesis), Manchester M60 1QD, United Kingdom: The University of Manchester; 2008.
- [50] Kröger H, Kornev N. Generation of divergence free synthetic inflow turbulence with arbitrary anisotropy. *Comput & Fluids* 2018;165:78–88. <http://dx.doi.org/10.1016/j.compfluid.2018.01.018>.